Assessment of RANS turbulence models on simplified geometries representative of turbine blade tip shroud flow

Fatih Uncu, Benjamin François, Nicolas Buffaz, Sébastien Le Guyader

ASSESSMENT OF RANS TURBULENCE MODELS ON SIMPLIFIED GEOMETRIES REPRESENTATIVE OF TURBINE BLADE TIP SHROUD FLOW

Fatih Uncu[*]
Safran Helicopter Engines
ONERA - The French Aerospace Lab
92190 Meudon, France
Email: fatih.uncu@onera.fr

Benjamin François[†]
ONERA - The French Aerospace Lab
DAAA, CFD Turbomachinery Team
92190 Meudon, France

Nicolas Buffaz[‡], **Sébastien Le Guyader**[‡]
Safran Helicopter Engines
Avenue Joseph Szydlowski
64511 Bordes, France

ABSTRACT

RANS turbulence models are assessed here in simulations of simplified configurations representative of geometries and flows found in tip shrouds of low-pressure turbines rotor blades. The complex flow inside a tip shroud is highly turbulent, its boundary layer separates at the sharp angled tangential fins and reattaches in the inter-fin cavity after a recirculation. The flow in the tip seal of the rotor blade, and the jet mixing flow at the exit of the shroud cause pressure losses and influence substantially the aerodynamic performance of the turbine. Such flows are quite challenging for the RANS models. The main aim of this paper is to assess the capability of the used turbulence models to predict tip shroud representative physics of detached, reattached and jet mixing flows. The simplified geometries consist of a backward facing step, a rib roughened channel and a jet in cross-flow. The Reynolds numbers of these configurations are close to those estimated in real tip shrouds. Experimental data are available in each case to evaluate the accuracy of the simulations and understand the behavior of the models. The evaluated turbulence models include several widely used eddy-viscosity models based on Boussinesq's hypothesis and a differential Reynolds stress model. Comparisons with measured components of the Reynolds stress tensor, turbulent kinetic energy and velocity profiles are presented. The velocity profiles are in good agreement with the measurements except in the recirculation regions, and eddy-viscosity models overpredict the level of experimental turbulent kinetic energy. Analysis of the strengths and weaknesses of the models for each flow are discussed.

Nomenclature

EARSM	Explicit Algebraic Reynolds Stress Model
DRSM	Differential Reynolds Stress Model
LES	Large Eddy Simulation
QCR	Quadratic Constitutive Relation
RANS	Reynolds Averaged Navier-Stokes
SST	Shear Stress Transport
D	Jet-pipe's diameter
ER	Step expansion ratio
H	Backward facing step height
h	Ribs height
r	Velocity ratio in jet flow
k	Turbulent kinetic energy
P_k	Turbulent kinetic energy production term
$R_{ij} = -\rho\overline{u'_i u'_j}$	ij-component of the Reynolds stress tensor
S_{ij}	Mean strain tensor
μ_t	Eddy viscosity
U_i	i^{th} component of the mean velocity
$\frac{D\phi}{Dt}$	Material derivative $\frac{\partial \phi}{\partial t} + \mathbf{U}.\nabla\phi$

INTRODUCTION

Reducing aerodynamic losses in multistage turbine is a constant focus for aircraft and helicopter engines manufacturers.

[*]PhD candidate [†]Research engineer [‡]Engineer

Cavity flows and tip shroud flows have both a significant contribution in the overall loss. Numerical simulation has become a major tool in turbomachinery design. Increased accuracy of the simulation method is required to estimate slight differences of losses between two geometries. On the other hand, a small computational time is essential for engineers during a design cycle. The RANS is still considered a good compromise between those two aspects. However, in regions of complex geometry presenting multiple separations, recirculations and reattachments, RANS models can fail to predict accurate results. The high turbulence level and important turbulence anisotropy in such non-equilibrium regions is still challenging for the classical eddy-viscosity models. Blade tip leakage and cavity flows belong to these problematic categories and turbulence modeling has to be wisely chosen.

Main studies on the cavity and labyrinth flows have used the $k-\omega$ SST turbulence model with a Kato-Launder limiter [1–3]. Perez *et al.* [4] have preferred a simpler one-equation Spalart-Allmaras model to simulate a single stage turbine with purge flow emanating from an upstream hub cavity. The authors noted that the simulation overpredicts the pressure losses between 20% and 40% in channel height, which corresponds approximately to the position of the passage vortex. Horwood *et al.* [1] find that the flow coming from the purge feeds this vortex. Spalart-Allmaras fails to reproduce accurately the interactions between the jet flow coming from the cavity and the main flow. Horwood *et al.* use the $k-\omega$ SST model and obtain results which are in good agreement with the experiment, except the overprediction of the purge flow egress which increases artificially the passage vortex and by consequence the pressure losses. The eddy-viscosity models are insensitive to curvatures [5] which could explain the lack of representativeness in cavity and tip shroud flows.

Gier *et al.* [6] used the $k-\omega$ Wilcox 1988 model to simulate a three-stage turbine with hub cavities and tip shrouds, as well as an ideal flow path case where the cavities are not modelled. The comparison to the experiment shows the importance of taking into account the cavities for the prediction of losses and isentropic efficiency. The cavity modelled simulation retrieves the experimental static pressure around blades but over-predicts locally the isentropic efficiency in the upper part of the channel (near tip shrouds), which is explained by the authors as a probable issue in the turbulence modelling leading to a lower radial mixing of the flow.

The off channel components, like tip shrouds, have complex geometries generating highly turbulent and anisotropic flows. The Boussinesq approach underestimates this anisotropy. Schmitt [7] introduces an indicator measuring the validity of the Boussinesq hypothesis. This indicator is an inner product of the Reynolds and the mean strain tensors. Gao *et al.* [8] have shown that for a linear eddy-viscosity model the indicator is close to zero (Boussinesq hypothesis fails completely) in the chute seal.

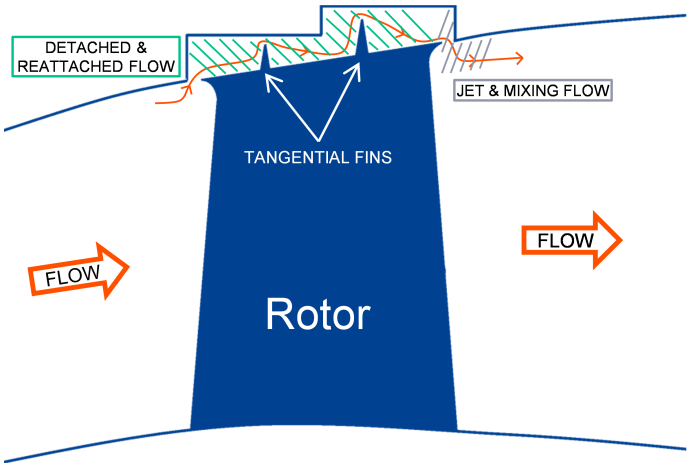

FIGURE 1: Tip shroud flow on a low-pressure turbine

The present work proposes to assess several turbulence models used in the aeronautical industry in very simple geometries that are representative of a tip shroud flow in turbine blade (Fig. 1). That will give us the possibility to understand how different models predict the detachment, reattachment and mixing flows in configurations that have a rich experimental database including Reynolds stresses. Such measurements are generally not possible in turbomachinery due to the complexity of setting up the appropriate experimental instrumentation. The conclusions are intended to be applicable to a tip shroud. In order to discuss the prediction capability of each model for the flow physics inside the clearance region, three configurations that isolate a detached, reattached and a mixing flow are studied. The detached flow, which appears after the entry in the tip shroud and at the tangential fins inside, is represented by the backward facing step of Driver and Seegmiller [9] and the rib roughened channel of Coletti *et al.* [10]. The behaviour of the models in the recirculation region before the reattachment is studied in these two configurations. The mixing process of the reduced velocity flow exiting the clearance area and the main flow, is represented by the jet in crossflow configuration of Andreopoulos and Rodi [11].

Often, turbulence models strengths and weaknesses are not well identified when applied to complex configurations with tip shroud and cavity flows. The originality of this work lays in the parallel comparison of the selected models on these three simple configurations enabling to extend the conclusions on a turbomachinery case.

First, the paper introduces the methodology. Then, the configurations and meshes are presented. Finally, velocity, turbulent kinetic energy and Reynolds stresses profiles are compared to the experiment and the results are discussed.

1 METHODOLOGY

1.1 RANS

Turbulence is modelled in RANS approach through the Reynolds stress tensor which appears in the Reynolds averaged momentum equation. This equation and the Reynolds averaged conservation of the mass equation for an incompressible flow (as it is the case for the three studied configurations) read:

$$\frac{\partial U_i}{\partial x_i} = 0 \tag{1}$$

$$\rho \frac{\partial U_i}{\partial t} + \rho U_j \frac{\partial U_i}{\partial x_j} = -\frac{\partial P}{\partial x_i} + \frac{\partial}{\partial x_j}\left(2\mu S_{ij} + R_{ij}\right) \tag{2}$$

with U, ρ, P, S_{ij}, and R_{ij} the Reynolds averaged values of the velocity, density, pressure, rate of strain tensor, and Reynolds stress tensor:

$$S_{ij} = \frac{1}{2}\left(\frac{\partial U_i}{\partial x_j} + \frac{\partial U_j}{\partial x_i}\right) \qquad R_{ij} = -\rho\overline{u_i' u_j'} \tag{3}$$

To close the equation system, additional equations are needed to solve the double correlations of the velocity fluctuations, i.e. the components of the Reynolds stress. The transport equation of the Reynolds stress components on which all RANS turbulence models are based reads:

$$\rho \frac{\partial \overline{u_i' u_j'}}{\partial t} + \rho U_k \frac{\partial \overline{u_i' u_j'}}{\partial x_k} = P_{ij} - \rho\varepsilon_{ij} + \phi_{ij} + D_{ij} + D^{\nu}_{ij} \tag{4}$$

where:

$P_{ij} = R_{ik}\frac{\partial U_j}{\partial x_k} + R_{jk}\frac{\partial U_i}{\partial x_k}$, is the production term

$\rho\varepsilon_{ij} = 2\mu\overline{\frac{\partial u_i'}{\partial x_k}\frac{\partial u_j'}{\partial x_k}}$, is the dissipation term

$\phi_{ij} = \overline{p'\left(\frac{\partial u_i'}{\partial x_j} + \frac{\partial u_j'}{\partial x_i}\right)}$, is the redistribution term

$D_{ij} = -\frac{\partial}{\partial x_k}\left(\rho\overline{u_i' u_j' u_k'} + \overline{p'\left(u_i'\delta_{jk} + u_j'\delta_{ik}\right)}\right)$, is the turbulent diffusion term

$D^{\nu}_{ij} = \frac{\partial}{\partial x_k}\left(\mu\frac{\partial \overline{u_i' u_j'}}{\partial x_k}\right)$, is the viscous diffusion term

Turbulence models

Boussinesq's turbulent viscosity hypothesis on which main two-equation models are based, links linearly R_{ij} to the turbulent kinetic energy k and the gradients of the mean flow S_{ij}:

$$R_{ij} = 2\mu_t S_{ij} - \frac{2}{3}\rho k\delta_{ij} \tag{5}$$

The three two-equation models that are utilized in the present work, $k-l$ Smith [12], $k-\omega$ Menter SST [13] and $k-\omega$ Wilcox 2006 [14], have a first equation on k which is half of the trace of the Eq. 4 and a second on the scale determining equation. The trace operator vanishes the redistribution term, ϕ_{ij}, for an incompressible flow leaving the production P_k, dissipation ε and diffusion D (pressure, molecular and turbulent transport) terms:

$$\rho\frac{Dk}{Dt} = \overbrace{R_{ij}\frac{\partial U_i}{\partial x_j}}^{P_k} - \overbrace{\rho\nu\overline{\frac{\partial u_i'}{\partial x_j}\frac{\partial u_i'}{\partial x_j}}}^{\rho\varepsilon} + \overbrace{\frac{\partial}{\partial x_j}\left[\mu\frac{\partial k}{\partial x_j} - \rho\frac{\overline{u_i' u_i' u_j'}}{2} - \overline{p' u_j'}\right]}^{D^{\nu}_k + D_k} \tag{6}$$

The contribution of the redistribution term, ϕ_{ij}, is significant as it redistributes the Reynolds stresses among the different directions. The absence of such term in two-equation models is not helping the non-isotropic nature.

Non-linear models such as the $k-\omega$ Hellsten EARSM model [15], reduce also the six-unknowns problem (components of R_{ij}) into two equations but add a non-linear term in Eq. 5. This non-linearity adds anisotropy in the turbulence. A similar attempt has been made with a simpler non-linear term in the Quadratic Constitutive Relation (QCR) correction for the Spalart-Allmaras model [16] and it has been extended to all the Boussinesq-based models:

$$R_{ij,QCR} = R_{ij} - C_{cr1}\left[O_{ik}R_{jk} + O_{jk}R_{ik}\right] \tag{7}$$

$$with \quad O_{ik} = 2\Omega_{ik}\Big/\sqrt{\frac{\partial U_m}{\partial x_n}\frac{\partial U_m}{\partial x_n}}, \quad \Omega_{ik} = \frac{1}{2}\left(\frac{\partial U_i}{\partial x_k} - \frac{\partial U_k}{\partial x_i}\right) \tag{8}$$

Reynolds stress transport models (RSM) are more complex as they have an equation per Reynolds stress tensor component and an equation for the dissipation scale. Just few (but nonetheless important) terms in the Eq. 4 necessitates modelling. Those are the dissipation, redistribution and turbulent diffusion terms. An additional transport equation is needed for the dissipation scale. The RSM model used in this study is the SSG/LRR-ω [17] and it uses the same dissipation scale equation as the one of Menter's.

1.2 Flow solver and Numerical parameters

Finite volume *elsA* solver [18] has been used in this study. The numerical scheme used for the simulations is the Roe upwind scheme [19] with a second order *van Albada* flux limiter [20]. The time integration scheme is the implicit Euler method.

The assessed turbulence models are the $k-l$ Smith, the SST Menter, the Wilcox 2006 and the RSM SSG/LRR-ω.

2 CONFIGURATIONS

Figure 2 shows the dimensions and boundary conditions of the three configurations. More details can be found in [9–11].

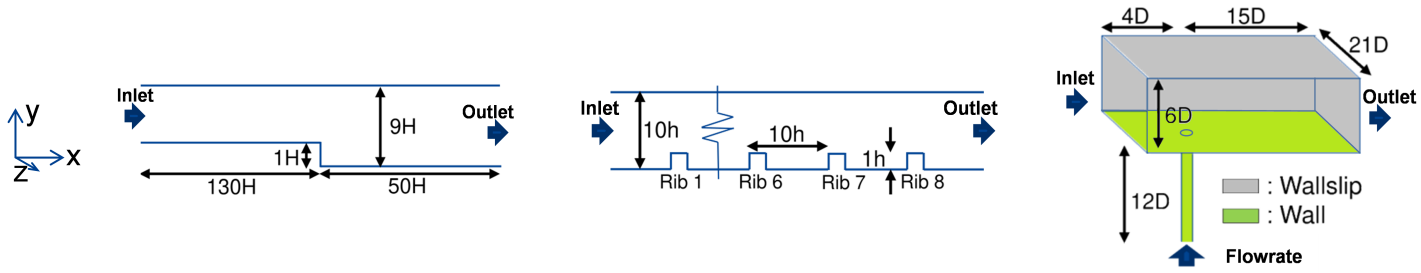

(a) (b) (c)

FIGURE 2: Dimensions and BCs of the (a) backward facing step, (b) rib roughened channel and (c) jet in crossflow

The backward facing step has a height, H, of one ninth of the channel height. The step expansion ratio is $ER = 9H/(9H - H) = 1.125$. It is preceded by a 130H long flat plate on which a turbulent boundary layer develops. A uniform total pressure is imposed at the inlet and the static pressure at the outlet of the computational domain. The exit static pressure is chosen so that the experimental Mach number is reached 4H upstream of the step. The ratio of the transverse dimension on the step height is 12: the configuration has been simplified into a 2D case.

The rib roughened channel is composed of 8 ribs of height h which are confined in a channel of height 10h. The ribs are transverse to the flow direction and are spaced of 10h. The inlet velocity, turbulent kinetic energy and turbulent dissipation scale are prescribed according to the profiles given by the measurements of Coletti *et al.* [10]. Similarly to the backward facing step, the flow at the symmetry plane of the channel is not influenced by the lateral walls (verified by a simulation) which allowed us to reduce the problem into a 2D flow. All the PIV measurements have been effectuated on the domain between the 6^{th} and 7^{th} rib, where the flow has reached a somewhat periodicity.

The jet in crossflow configuration is constituted of a pipe of diameter D which is 12D long and perpendicular to a flat plate. The velocity of the flow coming from the pipe is half of the crossflow: $r = V_{jet}/V_{crossflow} = 0.5$. The velocity and turbulent quantities profiles are prescribed at the main inlet. A flow rate condition is imposed in the jet inlet in order to respect $r = 0.5$ while on the outlet boundary condition the static pressure is equal to 1 atm. The flow regimes and the geometrical characteristics are presented and compared to a tip shroud flow in the Tab. 1.

	Tip shroud [21]	Step	Ribbed channel	Jet
Re	∼5000	36000	1500	20000
Ma	∼0.15	0.13	0.01	0.04
ER	∼4	1.125	1.11	-
r	<1	-	-	0.5

TABLE 1: Flow regimes of the three configurations

3 MESHES

For all of the three configurations, the first wall cell size verifies $y^+ < 1$ and the number of points in the boundary layer is at least equal to 20, with an expansion ratio of 1.13. The first two configurations that have been simplified into 2D cases have been meshed with a structured grid. An unstructured grid has been used for the jet in crossflow. Indeed, the unstructured approach is intended to be used in a tip shroud configuration. In the unstructured mesh, layers of pentahedral prisms are used on the walls of the flat plate and hexahedral prims on the walls of the pipe. The interior of the pipe is also composed of prisms and the main region of the crossflow area is made of tetrahedrons. Sectional views of the meshes are given in Fig. 3. The mesh size are respectively 120 000, 320 000 and 6 700 000 cells for the back step, rib roughened channel and jet in crossflow.

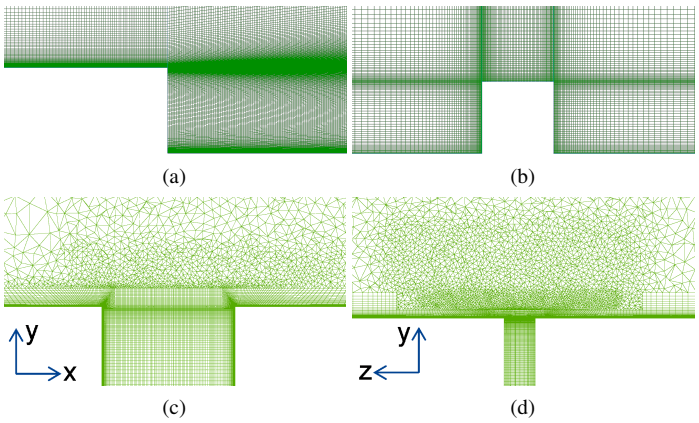

FIGURE 3: Sectional views of the meshes : (a) backward facing step, (b) rib roughened channel, and (c-d) jet in crossflow

4 RESULTS AND DISCUSSION

4.1 Simulations of detached and reattached flow

4.1.1 Backward facing step

Figure 4 shows the comparisons of streamwise velocity U, turbulent kinetic energy k, and Reynolds shear stresses $\overline{u'v'}$ between experimental measurements [9] and simulation results.

The first profile is 4H upstream of the step (at $x = -4H$), the two following are in the recirculation region (1H and 4H), the station at 6H is located just upstream of the reattachment point (which is measured experimentally at 6.26H) and finally, the last station is downstream of the recirculation (10H).

Firstly, all the models predict a boundary layer thickness at the upstream of the step ($x = -4H$) that is coherent with the experimental data: all the models predict a flow that reaches the step with an accurate U and k profiles. The following mean flow profiles are in quite good agreement with experimental data except for a slight overprediction of the shear stress level $\overline{u'v'}$. Notice however, that all ω-based models fail to predict the expected k-peak near the wall at $x = -4H$, unlike the $k-l$ model. Furthermore the LRR near-wall RSM closure is known to fail in correctly predicting the near wall anisotropy [22].

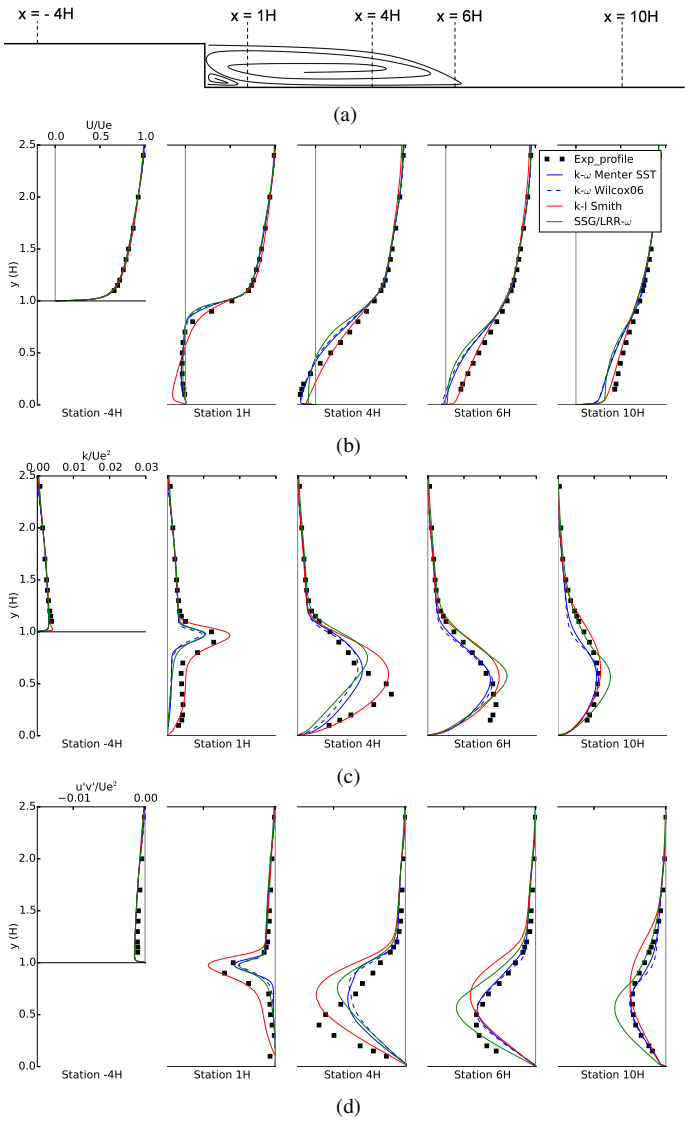

FIGURE 4: (a) Position of stations and profiles of normalized (b) streamwise velocity, (c) k and (d) $\overline{u'v'}$

The $k-l$ model based on a transport equation of a length scale stands out by over-predicting the backflow at x=1H just after the step. In this region a secondary recirculation is present. This recirculation is smaller and contrarotative compared to the main one. The analysis of the size of the corner recirculation shows that this model finds a smaller volume and length of recirculation compared to the others. The negative velocity at the station 1H is a result of this. Despite this default, it succeeds in catching up the experimental profiles in the following stations. It also predicts quite well turbulent quantities in the initial part of the mixing layer just downstream of the corner.

Another important point concerns the low velocity in the recirculation region of the models with a transport equation on specific dissipation rate, ω. It is particularly visible near the reattachment point ($x = 6H$). $k-\omega$ models present slower recovery in the vicinity of the reattachment point which mitigates downstream of the recirculation. This latency is accompanied with a bulge in the velocity profile between $y = 0H$ and $y = 1H$.

For the same $k-\omega$ models, the turbulent kinetic energy is too low near the wall at the first post-detachment station ($x = 1H$). Whereas the experimental data shows two peaks of energy at $y = 0.2H$ and $1H$, the simulations are not able to reproduce this behaviour (Fig. 4c). The measurements show that the near-wall peak increases at the center of the recirculation region (high turbulence intensity) and that the peak coming from the upstream boundary layer merges: the location of the peak's maximum lowers in the y direction. The same evolution is also visible in the Reynolds shear stress profiles (Fig. 4d).

The RSM $SSG/LRR-\omega$ model behaves like SST Menter and Wilcox 2006: low velocity at the end of the recirculation bulb and a near-wall bulge in the velocity profile. In addition, there is no velocity gradient in the near wall region in all the post-step stations. The experimental data close to the wall does not show this behaviour. The direct numerical simulation of Le *et al.* [23] on a backward facing step with an expansion ratio of 1.2, does not also show a zero U-gradient in the near wall region. The LRR model which is active in the near wall region is defective. Eisfeld and Rumsey [24] proposed a correction based on Yap's work on the transport equation for the dissipation scale, which improves the behaviour of the model near the reattachment point but has no impact on the global flow prediction.

Menter [25] compared different eddy-viscosity models on this configuration and showed that the Spalart model predicts too much backflow in the recirculation region like what we found for the $k-l$ Smith. He also found that none of the evaluated models (Spalart, Menter SST, $k-\varepsilon$ 2-L and RNG 2-L) accelerate enough near the wall to correctly predict the relaxation processes. The simulated flow is slower than the measured one: the recovery is too slow and so the reattachment is longer. He noticed that this behaviour is not only present in the backstep flow but in all sepa-

rated flows for the assessed models. This behaviour is generally observed in RANS models [26] which generally do not include lag-mechanisms to account for the detachment-reattachment hysteretic behaviour of turbulence. This strengthens our conclusions on the difficulties of capturing the correct streamwise velocity near the wall in the separated region.

Shih *et al.* [27] find also the bulge in the streamwise profiles with an EARSM model.

4.1.2 Rib roughened channel

Fransen *et al.* [28] have studied the rib roughened channel using the $k-l$ Smith model and showed that RANS simulation misses locally the fluid acceleration and recirculation at the top of ribs. Some wall-resolved LES simulations have been carried out on this configuration and they show very good agreement with the experiment reproducing very well all the velocity and turbulence profiles [29–31].

The flow with the presence of a rib is very close to what is seen in the precedent case (Fig. 5). The two contrarotative recirculations in the downstream of the rib are the same as in the backward facing step. The following ascending step is an obstacle for the flow and a third recirculation is created at the left bottom corner of the 7^{th} rib. A last recirculation region is visible at the top of the rib where there is not enough space to recreate an attached boundary layer.

Figure 5 shows that the main recirculations are reproduced by all the models except in the downstream corner and above the rib (recirculations 1 and 4). Indeed the flow over the rib has an attached boundary layer and the downstream corner recirculation is too small to be visible. Only the RSM model predicts a small bulb at the top of the rib but it is very marginal compared to

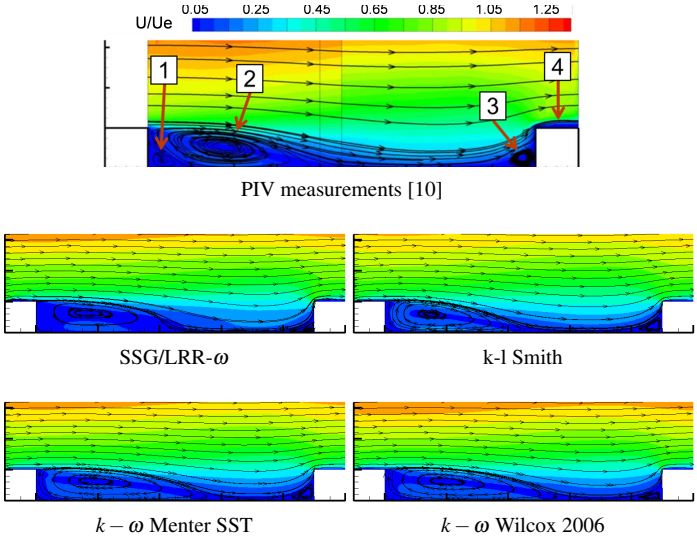

FIGURE 5: Normalized velocity fields between 6^{th} and 7^{th} ribs

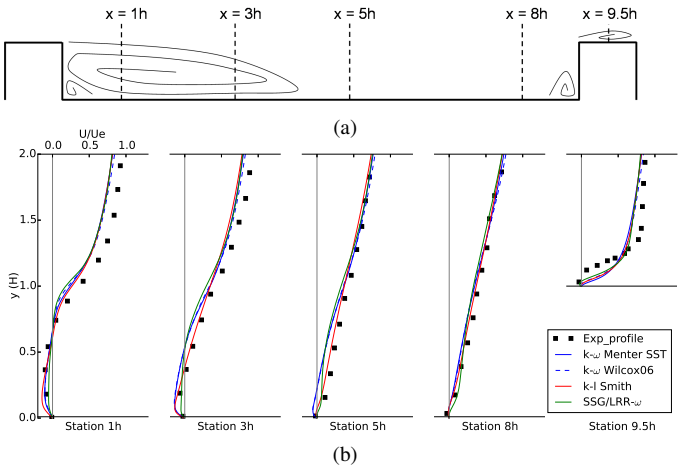

FIGURE 6: (a) Position of stations and (b) normalized streamwise velocity

experimental data.

The main recirculation is longer for the $k-\omega$ Menter and Wilcox models. That was also observed in the backward facing step but is amplified in this configuration due to the error accumulation of the reattachment length's misprediction. These two models have an SST limiter modifying the definition of the eddy viscosity: $\mu_t = k/\omega_{eff}$ with ω_{eff} greater or equal to ω. Reducing the eddy viscosity leads to less Reynolds stress and so to a longer recirculation bulb. This result is also found by Wilcox [32], where the increase of the coefficient C_{lim} in the SST formulation of the Wilcox 2006 model extends the reattachment length.

The velocity profiles are presented in the Fig. 6. No significant differences are observed between the $k-\omega$ and $SSG/LRR-\omega$ models. Like in the backward facing step case, a delay in the recirculation region between the two ribs appears for these models. All the calculations underpredict the streamwise velocity between $y = 0h$ and $y = 2h$. The Smith model marks a difference by its capacity to well predict the near-wall mean flow. The downstream recirculation (number 2 in Fig. 5) is well reproduced. Finally, at $x = 9.5h$, the experiments show a separated boundary layer, while a new boundary layer starts to develop in the upper part of the ribs in the simulations. The error on the velocity between the two ribs is also due to the absence of this separation. Beyond that, all of the turbulence models are able to predict a mean flow dynamics which is in agreement with the measurements.

Turbulence fields

Figure 7 presents the normalized shear stress, Tu_x and Tu_y with $Tu_i = \sqrt{\overline{u_i'^2}}/U_0$. The measurements show a plume of $\overline{u'u'}$ in the upper part of the ribs which is the signature of the separated boundary layer. The maximum $\overline{u'u'}$ is reached at the downstream top corner of the rib, where a shear layer starts to develop. The

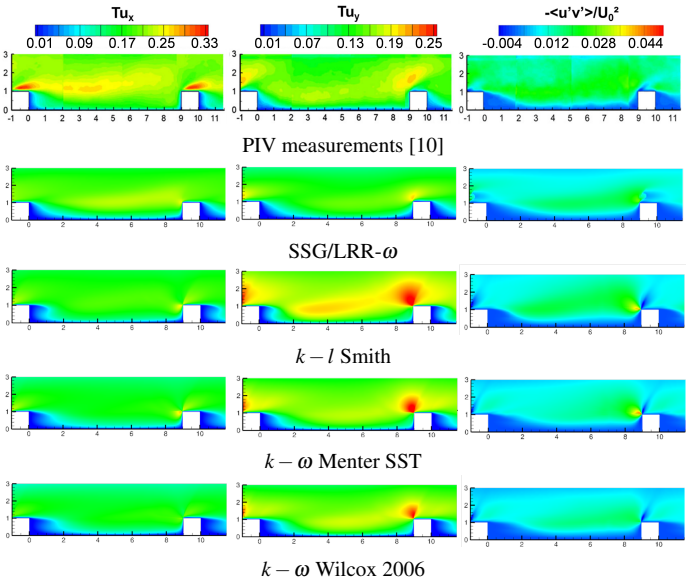

FIGURE 7: Tu_x, Tu_y and normalized Reynolds shear stress fields

peak of Tu_y is reached in the upstream corner, where the flow is accelerated due to the streamline curvature. Tu_x, i.e. the axial velocity fluctuations, is inhibited in the downstream side because of the presence of the obstacle. Finally, according to Coletti *et al.* [10], the main production source of $\overline{u'v'}$ is the shear layer generated above the ribs.

In our simulations the high Tu_x area is not reproduced at the top of the obstacle. Assuming that it is the footprint of the recirculation in this location, it is normal that the simulations do not predict it knowing that the separated boundary layer is not captured. A second default is the anomaly on the overproduction of the $\overline{v'v'}$ stress at the upstream top corner. This behaviour is present in all the three eddy-viscosity models. The exact production term of the turbulent kinetic energy is $P_k = R_{ij}\frac{\partial U_i}{\partial x_j}$. For an incompressible flow and with the Boussinesq hypothesis, this term simplifies into $P_k = \mu_t S^2$ with $S = \sqrt{2S_{ij}S_{ij}}$ and $S_{ij} = 1/2\left(\partial U_i/\partial x_j + \partial U_j/\partial x_i\right)$. The production term field, P_k, computed with the Menter SST model is presented in the Fig. 8. The maximum of this production is reached at the same location as the anomaly of Tu_y. It is therefore a defect of the Boussinesq hypothesis which is the well-known stagnation point anomaly [33] which is characterized by a turbulence overproduction in high acceleration and deceleration regions. The RSM model (Fig. 7) does not reproduce this anomaly: the production term is exempt from modeling. One way to solve this anomaly is to change the production term with the Kato-Launder modification [34]: $P_k = \mu_t S\Omega$ with $\Omega = \sqrt{2\Omega_{ij}\Omega_{ij}}$ and $\Omega_{ij} = 1/2\left(\partial U_i/\partial x_j - \partial U_j/\partial x_i\right)$, or to use the vorticity source term [35]: $P_k = \mu_t \Omega^2$. As it can be seen in the Fig. 8, these two other formulations of the production terms help indeed to reduce the anomaly. In this zone, a high $\partial U/\partial x$ gradient contributes to S which leads to a turbulence overproduction. This gradient disappears in the vorticity term. In our

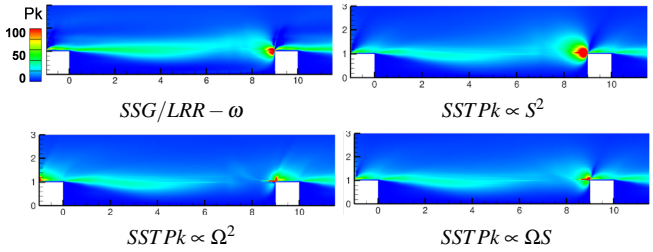

FIGURE 8: Normalized k production term fields, P_k

case this change does not deteriorate the solution elsewhere. Indeed, in a boundary layer S and Ω have the same dominant term: $\partial U/\partial y$. It has to be noted that the removal of this anomaly does not have any significant influence on the mean flow solution.

The Reynolds shear stress which is the dominant Reynolds stress component in the momentum equations of a turbulent boundary layer, must be well-modeled. Figure 7 shows that all the models predict a lower $\overline{u'v'}$ than the measurements. The RSM simulation gives the most accurate distribution of $\overline{u'v'}$. The four other models show a filet of negative stress just after the leading edge. A zone of positive stress in the upstream of the leading edge is visible for the Smith and Menter models. It is the main difference between the Menter and Wilcox models. This difference could be explained by the SST limiter which is a function of $\sqrt{\Omega_{ij}\Omega_{ij}}$ for the former and of $\sqrt{S_{ij}S_{ij}}$ for the latter. Given that S is greater in the leading edge area, the SST limiter will further decrease μ_t and consequently $\overline{u'v'}$ in the case of the Wilcox model. The same argument explains why the Tu_x pocket at the same area is not present for the Wilcox model and that the Tu_y pocket is lower than the Menter SST simulation. The upstream anomaly is less visible with the Wilcox 2006, the difference being in the level of eddy viscosity. For this configuration, the SST limiter used by Wilcox 2006 is preferable to the one presented in Menter's model [13].

In addition, three-dimensional RANS simulations have been carried out to understand the importance of turbulence anisotropy in the creation of "lateral" secondary structures. The LES simulation of Grosnickel [31] shows that along the channel, parietal structures are created. These are Taylor-Görtler type vortices. These structures of very low speed are shown in the Fig. 9 in the plane between the 6^{th} and 7^{th} ribs at a constant $x/h = 4.5$. The non-linear EARSM Hellsten model was also evaluated here to see how it behaves compared to a linear model. The RSM and EARSM models are able to create those structures while an eddy-viscosity model like Menter cannot. The two other Boussinesq models that are not shown here behaves the same way as the $k-\omega$ Menter SST. The main difference is the anisotropy being naturally present in the former models while a classical Boussinesq model is based on a linear constitutive relation. The addition of a non-linear term through the QCR correction in this relation is here helping to reproduce similar structures. The

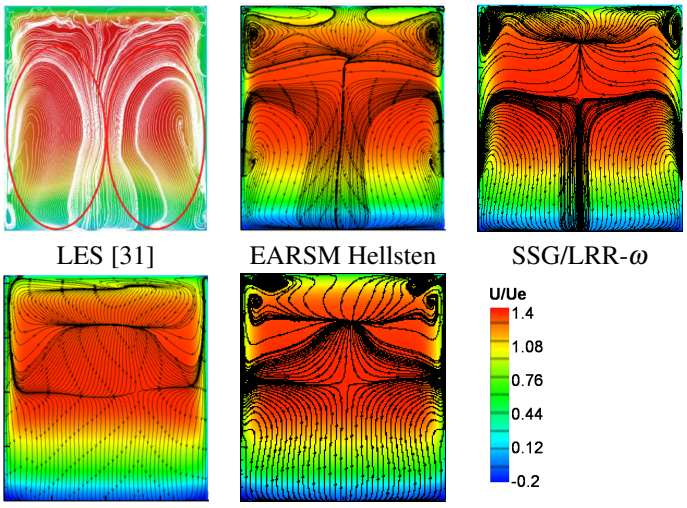

LES [31] EARSM Hellsten SSG/LRR-ω

$k-\omega$ Menter $k-\omega$ Menter QCR

FIGURE 9: Streamlines and U on a plane at constant $x/h = 4.5$

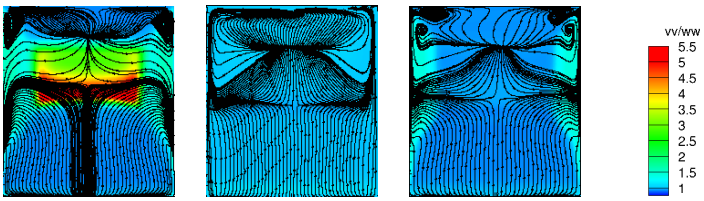

SSG/LRR-ω $k-\omega$ Menter $k-\omega$ Menter QCR

FIGURE 10: $\overline{v'v'}/\overline{w'w'}$, on a plane at constant $x/h = 4.5$

anisotropy of turbulence, measured here by the ratio $\overline{v'v'}/\overline{w'w'}$, is primordial in the generation of such streamlines. The non-linearity of the QCR correction seems to create an anisotropy closer to the RSM simulation (Fig. 10) and is therefore recommended in simulations where parietal structures and turbulence anisotropy are important. The simulation without QCR shows Reynolds stresses that are quasi equivalent in the directions y and z, while there is a ratio of more than 5 for the RSM model. The anisotropy of the EARSM model (which is not presented) does not reach this ratio, but near the left and right walls $\overline{v'v'} >> \overline{w'w'}$ which causes the apparition of the recirculations. The same underprediction of anisotropy applies also to the QCR.

4.2 Simulation of mixing flow

At very low velocity ratios, which is the case here, the flow inside the pipe starts to bend before the exit plane [36]. At the pipe outlet, the streamlines are totally aligned with the crossflow: the momentum being half of the main flow, the jet cannot resist and is dragged by the orthogonal flow. The main flow bends to get around the flow coming from the pipe. A complex topology is created: the main flow is deviated partly above and at each sides of the "obstacle". A horseshoe vortex and a CVP (Counter-rotating Vortex Pair) are the main secondary structures that develop (view Fig. 11). These vortices contribute to the mixing process and cause pressure losses. In film-cooling jet flows, they amplify the thermal exchanges.

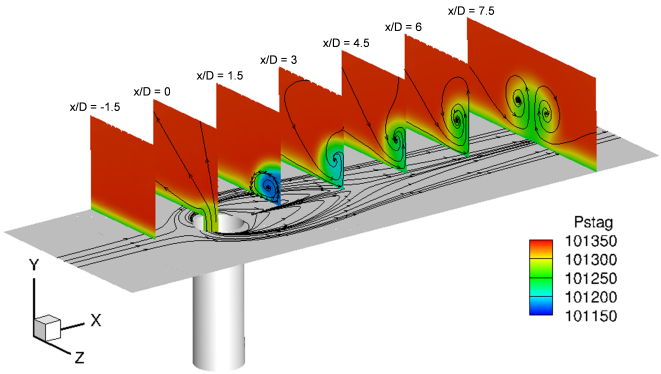

FIGURE 11: Streamlines and total pressure in the jet in crossflow

4.2.1 Flow dynamics of the mean flow

Streamwise velocity U

A deceleration above the pipe exit (which is located between $x/D = -0.5$ and $x/D = 0.5$) in the symmetry plane $z/D = 0$ (first 5 stations) is visible before an acceleration due to the dragging of the main flow (Fig. 12a). High velocity gradients are present at $x/D = 1$ and $x/D = 2$. These gradients connect the low near-wall velocities and the external U_e flow. It is shown that the $\partial U/\partial y$ gradient is the main term contributing to the production of turbulence in the wake area of the jet.

At $z/D = 0.5$, the velocities are greater than on the symmetry plane where the wake acts like an obstacle which slows down the flow. The velocity is increasing near the wall. The explanation is the deviation and acceleration of the main flow around the wake region [11].

The simulations are able to reproduce the streamwise velocity profiles on the first stations (until $x/D = 0.5$). Indeed, the bended jet flow does not influence the crossflow in that region. Downstream the behaviour of the Smith model which fits nearly all the experimental dots at $x/D = 0.5$ and $x/D = 1$ ($z/D = 0.5$) is remarkable. The same is visible on the symmetry plane, where the other two models underestimate U, the k-l Smith model captures the experimental profile downstream of the jet exit and in the wake region.

On the other hand, the same model predicts velocity profiles that seem to be smoothed and the gradients erased especially in the inflection points at $x/D = 2$. This behaviour can be associated to the level of eddy viscosity produced by this model.

The similarity of the flow dynamics predicted by the Menter SST and SSG/LRR-ω should be noted. They both show discrepancies in the plane $z/D = 0.5$ from $x/D = 0.25$ to $x/D = 2$. A recirculation, which is not proven by the experiment, is predicted

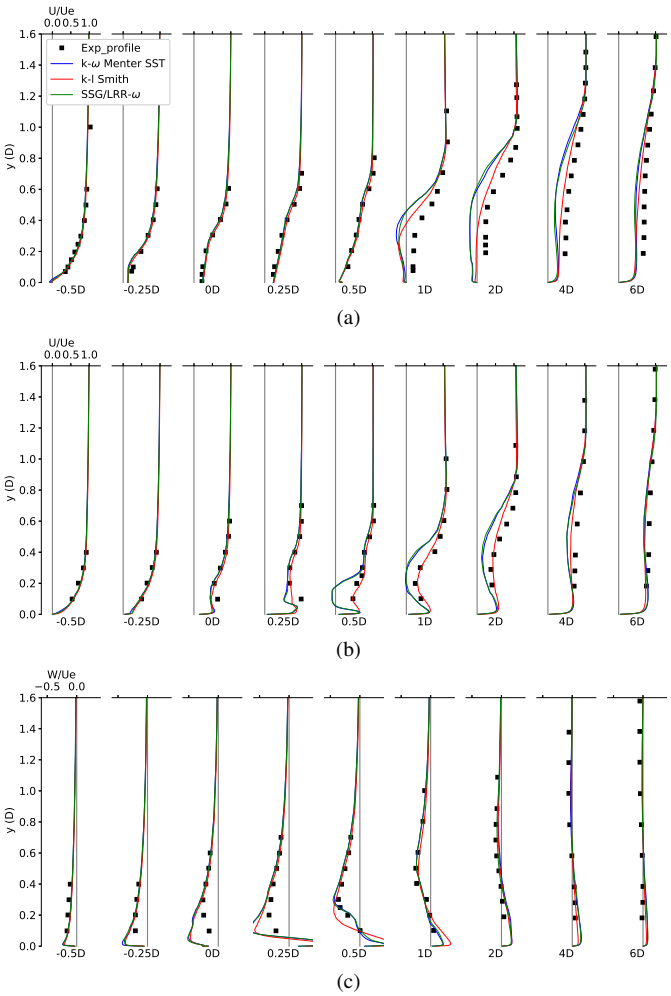

FIGURE 12: Normalized streamwise velocity U at (a) $z/D = 0$, (b) $z/D = 0.5$, and (c) transverse velocity W at $z/D = 0.5$

and makes the flow slower in that region.

Mengler *et al.* [37] who studied the same jet in crossflow with LES and two different second order turbulence models (SSG and Jones-Musonge), showed the same discrepancies at stations $x/D = 1$ and $x/D = 2$ for the streamwise velocity.

Transverse velocity W

The transverse component of the velocity is negative on the first stations. The main flow moves away from the symmetry plane from either sides of the jet. Downstream W becomes positive: the low pressure region generated by the wake attracts the flow towards the symmetry plane.

All the simulations overestimate the distancing from the symmetry plane at the jet exit area. On the plane of the downstream outlet corner ($x/D = 0.5$) and on the following profile, the k-ω and SSG/LRR-ω models capture the good transverse velocity profiles while the Smith model predicts too much lateral spread between $y/D = 0.1$ and $y/D = 0.3$.

4.2.2 Turbulence fields

Turbulent kinetic energy

The main term contributing to the production of turbulence, P_k, is $-\rho\overline{u'v'}\partial U/\partial y$. The velocity gradient $\partial U/\partial y$ pilots the turbulence production in the mixing region. This is easily verified by checking the correlation of the peaks positions of this gradient and k profiles. Another gradient participating to the production is $\partial W/\partial z$. Downstream, the gradients and the turbulent kinetic energy dissipate. The peaks of k are convected to the near-wall region.

On the symmetry plane, the two eddy-viscosity models overpredict the turbulent kinetic energy in the wake region of the jet (Fig. 13a). This over-evaluation is all the more important with the k-l Smith model as k is almost three times greater than what is measured at $x/D = 1$ and $x/D = 2$. The RSM model retrieves the experimental level of k and the position of the peak is also well-predicted. However, none of the models reproduce the convection of k towards the flat plate in the last stations ($x/D = 4$ and $x/D = 6$).

At $z/D = 0.5$, again the Smith model overestimates k as early as $x/D = 0$. The double peak of k (also present in the gradient $\partial U/\partial y$) is retrieved for the k-ω and RSM models but with much lower levels of energy. A third peak is also observed for these two models ($x/D = 0.25$ and $x/D = 1$) near the wall. Andreopoulos [11] notes also the presence of this peak out of the measurement probe area.

The Smith model, which produces too much turbulence in the mixing region, predicts a level of k which is equivalent to the measurements at $x/D = 0.25$ and $x/D = 0.5$ in the $z/D = 0.5$ plane (Fig. 13b). It corresponds to the region where the mean flow dynamics is remarkably well predicted by the same model. The Smith model differentiates itself in the downstream corner of the jet exit. One conclusion is that even if the turbulence kinetic energy is overevaluated in the mixing region (jet wake), the flow dynamics will be mainly impacted by the prediction of k just after the jet exit plane.

$\overline{u'v'}$ stress

The evolution of $\overline{u'v'}$ is very similar to that of k. Indeed the prevailing production term in P_k includes $\overline{u'v'}$. The gradient $\partial U/\partial y$ is also the main production mechanism of the Reynolds shear stress through the term: $-\rho\overline{v'v'}\partial U/\partial y$. We can notice on the measurements that the maximum of $\overline{u'v'}$ is reached further downstream than k's. That could be explained by the fact that the production does not depend only on the precedently cited gradient but also on $\overline{v'v'}$ which is convected from upstream.

Just like the turbulent kinetic energy, the Reynolds shear stresses $\overline{u'v'}$ are also overestimated by the Menter SST and k-l Smith models from $x/D = -0.2$ to $x/D = 2$. Mengler *et al.* [37] finds that even LES simulations show discrepancies and overpredict the level of $\overline{u'v'}$ stresses. In contrast, the RSM SSG/LRR-ω simulation performs very well in retrieving the

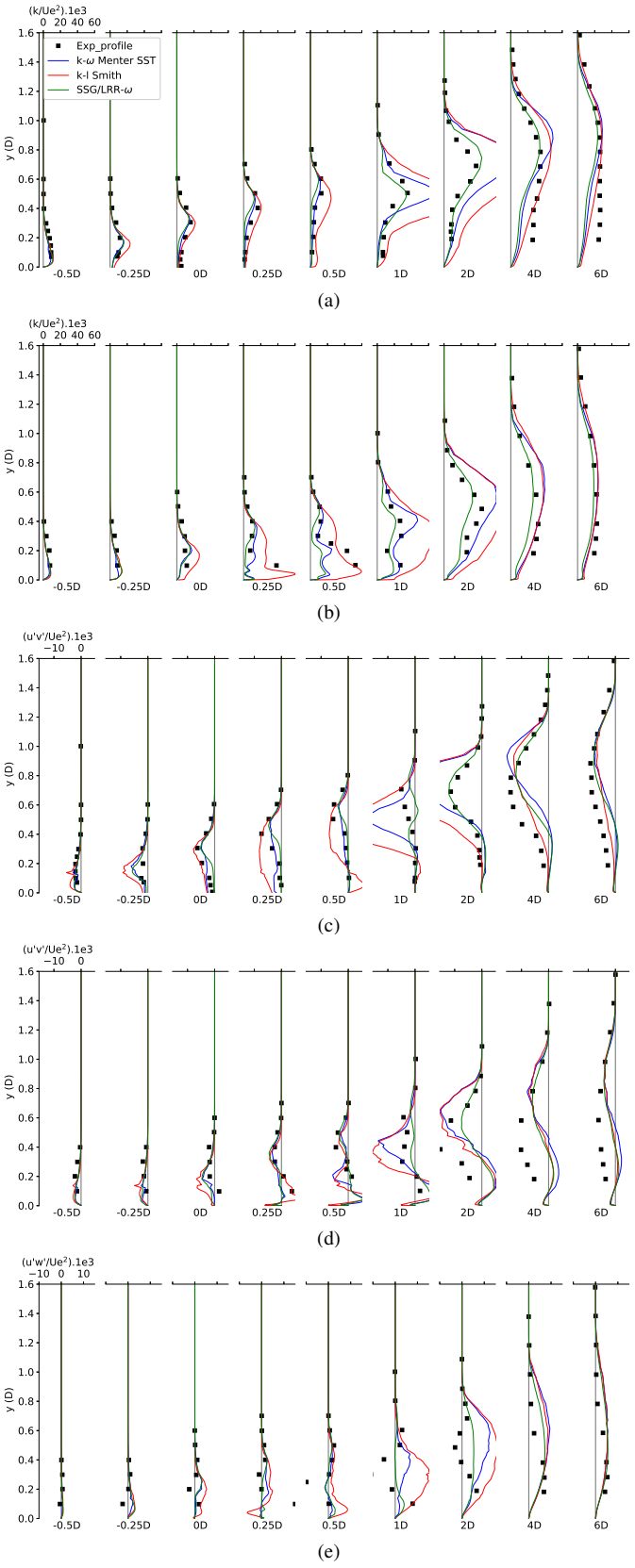

FIGURE 13: Normalized k at (a) $z/D = 0$ and (b) $z/D = 0.5$, $u'v'$ at (c) $z/D = 0$ and (d) $z/D = 0.5$, and (e) $u'w'$ at $z/D = 0.5$

same $\overline{u'v'}$ level as in the measurements.

$\overline{u'w'}$ stress

The $u'w'$ stresses pilot the lateral spread of the jet wake. The RANS momentum equation projected on the x and z axis show that the derivatives of $\overline{u'w'}$ in the spreading directions ($\partial/\partial x$ and $\partial/\partial z$) modify to the first order the dynamics of the flow in these two directions.

The main gradients contributing to the production of $\overline{u'w'}$ are $\partial U/\partial z$ and $\partial W/\partial y$ according to the decomposition of the production term:

$$\begin{aligned} P_{xz} = &-\rho\overline{u'u'}\frac{\partial W}{\partial x} - \rho\overline{u'v'}\frac{\partial W}{\partial y} - \rho\overline{u'w'}\frac{\partial W}{\partial z} \\ &-\rho\overline{w'u'}\frac{\partial U}{\partial x} - \rho\overline{w'v'}\frac{\partial U}{\partial y} - \rho\overline{w'w'}\frac{\partial U}{\partial z} \end{aligned} \tag{9}$$

Among these terms, $\overline{u'w'}$, $\overline{w'v'}$ and the gradient $\partial W/\partial x$ are very small and negligible. The measured stresses are quasi zero in the first stations because the main gradients in Eq. 9, i.e. $\partial U/\partial z$ and $\partial W/\partial y$ are also very small at the location of the jet exit. Once these gradients start growing, the production and the level of $\overline{u'w'}$ increase.

Both eddy-viscosity models and the evaluated RSM model are not able to give a realistic simulation of $\overline{u'w'}$ evolution. Indeed, from $x/D = 0.5$ to $x/D = 2$ the simulations predict a positive peak where the experiment shows negative stresses. Andreopoulos and Rodi [11] explain it for the eddy-viscosity models by the fact that Boussinesq's constitutive relation links this stress to $\partial U/\partial z$ and $\partial W/\partial x$ but not $\partial W/\partial y$. However in our case, the RSM model which has its own transport equation for $\overline{u'w'}$ also does not perform well.

5 CONCLUSIONS

The present study focuses on the assessment of turbulence models in turbine tip shroud flow representative configurations.

For detached and reattached flows, all the evaluated models show good agreement with the experimental mean profiles. However, it is seen that $k-\omega$ models as well as the $SSG/LRR-\omega$ model have a latency in the velocity profiles in the recirculation region. The prediction of the flow recovery at the end of the recirculation is not accurate in the near wall region. The $k-\omega$ models find a recirculation length which is longer than expected. It can be solved by preferring a model without an SST limiter like the Menter BSL model. The RSM model has a zero-gradient streamwise velocity profile in the near wall region of the recirculation. This behaviour can be locally improved by a Yap correction but has no impact on the global flow prediction. And finally, the turbulence length transporting model underpredicts the secondary recirculation in the downstream corner of the step and overpredicts the backflow.

The RSM SSG/LRR-ω is the model that fits the best the experimental mean turbulence profiles. Boussinesq models overpredict the turbulent kinetic production due to the stagnation point anomaly. This can be overcome by a modification of the production term with a vorticity source term that reduces the anomaly just upstream of the rib.

The anisotropy of turbulence has shown to be important in the prediction of lateral-wall related secondary structures. This anisotropy being naturally present in the RSM and EARSM models, they are able to create those structures while an eddy-viscosity model cannot do it without a QCR correction. However, this better prediction of the RSM is at a higher cost of calculation. The computational time per iteration per cell is $\sim 20\%$ longer than a classical 2-equation model.

For the jet in crossflow, the model that fits the best the mean profiles is the $k-l$ Smith while for turbulence profiles it is still the RSM. The Smith model predicts a correct mean velocity thanks to a good prediction of the turbulence locally at the jet exit, but everywhere else, it largely overpredicts the turbulence level inside the mixing region. Finally the Menter SST and $SSG/LRR-\omega$, which share a nearly common dissipation transport equation and blending functions, show a very similar flow dynamics solution.

It would be now interesting to see if these conclusions are retrieved and if the RSM, which shows the best agreement with turbulence measurements and predicts an accurate mean flow dynamics, performs also well in a turbomachinery configuration. This is the subject of ongoing research.

ACKNOWLEDGMENT

The authors wish to thank Georges Gerolymos (Sorbonne University), Raphael Barrier (ONERA) and Jacques Demolis (Safran Helicopter Engines) for the fruitful discussions on turbulence modeling and on the results analysis.

REFERENCES

[1] Horwood, J. T. M., Hualca, F. P., Wilson, M., Scobie, J. A., Sangan, C. M., Lock, G. D., Dahlqvist, J., and Fridh, J., 2020. "Flow Instabilities in Gas Turbine Chute Seals". *Journal of Engineering for Gas Turbines and Power,* ***142***(2), 01. 021019.

[2] Jones, R. R., Pountney, O. J., Cleton, B. L., Wood, L. E., Schreiner, B. D. J., Figueiredo, A. J. C., Scobie, J. A., Cleaver, D. J., Lock, G. D., and Sangan, C. M., 2019. "An Advanced Single-Stage Turbine Facility for Investigating Non-Axisymmetric Contoured Endwalls in the Presence of Purge Flow". Vol. Volume 2B: Turbomachinery of *Turbo Expo: Power for Land, Sea, and Air*. V02BT40A004.

[3] Wang, C.-Z., Mathiyalagan, S. P., Johnson, B. V., Glahn, J. A., and Cloud, D. F., 2013. "Rim Seal Ingestion in a Turbine Stage From 360 Degree Time-Dependent Numerical Simulations". *Journal of Turbomachinery,* ***136***(3), 09. 031007.

[4] Perez, E., Schmitz, J. T., Jaffa, N. A., Jemcov, A., Cameron, J. D., and Morris, S. C., 2019. "Detailed Experimental Measurement and RANS Simulation of a Low Pressure Turbine With High Lift Blading". Vol. Volume 2B: Turbomachinery of *Turbo Expo: Power for Land, Sea, and Air*. V02BT40A029.

[5] Arolla, S. K., and Durbin, P. A., 2013. "Modeling Rotation and Curvature Effects within Scalar Eddy Viscosity Model Framework". *International Journal of Heat and Fluid Flow,* ***39***, pp. 78–89.

[6] Gier, J., Stubert, B., Brouillet, B., and de Vito, L., 2003. "Interaction of Shroud Leakage Flow and Main Flow in a Three-Stage LP Turbine". *Journal of Turbomachinery,* ***127***(4), 03, pp. 649–658.

[7] Schmitt, F. G., 2007. "About Boussinesq's Turbulent Viscosity Hypothesis: Historical Remarks and a Direct Evaluation of its Validity". *Comptes Rendus Mécanique,* ***335***(9-10), pp. 617–627.

[8] Gao, F., Poujol, N., Chew, J. W., and Beard, P. F., 2018. "Advanced Numerical Simulation of Turbine Rim Seal Flows and Consideration for RANS Turbulence Modelling". Vol. Volume 5B: Heat Transfer of *Turbo Expo: Power for Land, Sea, and Air*. V05BT15A005.

[9] Driver, D. M., and Seegmiller, H. L., 1985. "Features of a Reattaching Turbulent Shear Layer in Divergent Channelflow". *AIAA Journal,* ***23***(2), pp. 163–171.

[10] Coletti, F., Maurer, T., Arts, T., and Di Sante, A., 2012. "Flow Field Investigation in Rotating Rib-roughened Channel by Means of Particle Image Velocimetry". *Experiments in fluids,* ***52***(4), pp. 1043–1061.

[11] Andreopoulos, J., and Rodi, W., 1984. "Experimental Investigation of Jets in a Crossflow". *Journal of Fluid Mechanics,* ***138***, p. 93–127.

[12] Smith, B., 1994. "A Near Wall Model for the k-l Two-equation Turbulence Model". In Fluid Dynamics Conference, p. 2386.

[13] Menter, F. R., 1994. "Two-equation Eddy-viscosity Turbulence Models for Engineering Applications". *AIAA Journal,* ***32***(8), pp. 1598–1605.

[14] Wilcox, D., 2006. *Turbulence Modeling for CFD*. Turbulence Modeling for CFD. DCW Industries.

[15] Hellsten, A., 2005. "New advanced k-w Turbulence Model for High-Lift Aerodynamics". *AIAA journal,* ***43***(9), pp. 1857–1869.

[16] Spalart, P., 2000. "Strategies for Turbulence Modelling and Simulations". *International Journal of Heat and Fluid Flow,* ***21***(3), pp. 252–263.

[17] Cécora, R.-D., Radespiel, R., Eisfeld, B., and Probst, A., 2015. "Differential Reynolds-Stress Modeling for Aeronautics". *AIAA Journal,* ***53***(3), pp. 739–755.

[18] Cambier, L., Heib, S., and Plot, S., 2013. "The Onera elsA CFD Software: Input from Research and Feedback from Industry". *Mechanics & Industry,* ***14***(3), pp. 159–174.

[19] Roe, P., 1981. "Approximate Riemann Solvers, Parameter Vectors, and Difference Schemes". *Journal of Computational Physics,* ***43***(2), pp. 357–372.

[20] van Albada, G., van Leer, B., and Roberts, 1982. "A Comparative Study of Computational Methods in Cosmic Gas Dynamics". *Astronomy and Astrophysics,* ***108***, 04, pp. 76–84.

[21] , 2016. Effects of Tip Shroud Geometries on Low-Pressure Turbine Performance, Vol. Volume 2B: Turbomachinery of *Turbo Expo: Power for Land, Sea, and Air*. V02BT38A001.

[22] Jones, L., Gaskell, P., Thompson, H., Gu, X., and Emerson, D., 2005. "Anisotropic, Isothermal, Turbulent Swirling Flow in a Complex Combustor Geometry". *International journal for numerical methods in fluids,* ***47***(10-11), pp. 1053–1059.

[23] Le, H., Moin, P., and Kim, J., 1997. "Direct Numerical Simulation of Turbulent Flow over a Backward-facing Step". *Journal of Fluid Mechanics,* ***330***, p. 349–374.

[24] Eisfeld, B., and Rumsey, C. L., 2020. "Length-scale Correction for Reynolds-stress Modeling". *AIAA Journal,* ***58***(4), pp. 1518–1528.

[25] Menter, F. R., 1996. "A Comparison of Some Recent Eddy-Viscosity Turbulence Models". *Journal of Fluids Engineering,* ***118***(3), 09, pp. 514–519.

[26] Gerolymos, G., Lo, C., Vallet, I., and Younis, B., 2012. "Term-by-term Analysis of Near-wall Second-moment Closures". *AIAA journal,* ***50***(12), pp. 2848–2864.

[27] Shih, T.-H., Zhu, J., and Lumley, J. L., 1995. "A New Reynolds Stress Algebraic Equation Model". *Computer methods in applied mechanics and engineering,* ***125***(1-4), pp. 287–302.

[28] Fransen, R., Gourdain, N., and Gicquel, L. Y. M., 2012. Steady and Unsteady Modeling for Heat Transfer Predictions of High Pressure Turbine Blade Internal Cooling, 06.

[29] Grosnickel, T., Duchaine, F., Gicquel, L. Y. M., and Koupper, C., 2017. "Large Eddy Simulations of Static and Rotating Ribbed Channels in Adiabatic and Isothermal Conditions". Vol. Volume 5A: Heat Transfer of *Turbo Expo: Power for Land, Sea, and Air*.

[30] Fransen, R., Vial, L., and Gicquel, L. Y., 2013. "Large Eddy Simulation of Rotating Ribbed Channel". In Turbo Expo: Power for Land, Sea, and Air, Vol. 55140, American Society of Mechanical Engineers, p. V03AT12A033.

[31] Grosnickel, T., 2019. "Simulations des grandes échelles pour la prédiction des écoulements de refroidissement des pales de turbines". PhD thesis, Toulouse INP.

[32] Wilcox, D. C., 2008. "Formulation of the k-w Turbulence Model Revisited". *AIAA journal,* ***46***(11), pp. 2823–2838.

[33] Durbin, P. A., 1996. "On the k-3 Stagnation Point Anomaly". *International Journal of Heat and Fluid Flow,* ***17***, pp. 89–90.

[34] Kato, M., and Launder, B., 1993. "The Modelling of Turbulent Flow Around Stationary and Vibrating Square Cylinders".

[35] Menter, F. R., 1992. "Improved Two-equation k-omega Turbulence Models for Aerodynamic Flows". *Nasa Sti/recon Technical Report N,* ***93***, p. 22809.

[36] Andreopoulos, J., 1982. "Measurements in a Jet-Pipe Flow Issuing Perpendicularly Into a Cross Stream". *Journal of Fluids Engineering,* ***104***(4), 12, pp. 493–499.

[37] Mengler, C., Heinrich, C., Sadiki, A., and Janicka, J., 2001. "Numerical Prediction of Momentum and Scalar Fields in a Jet in Cross Flow: Comparison of LES and Second Order Turbulence Closure Calculations". In Second Symposium on Turbulence and Shear Flow Phenomena, Begel House Inc.